RSC Advances

PAPER

View Article Online
View Journal | View Issue

Cite this: *RSC Adv.*, 2025, **15**, 39566

Nanoporous ZnO/SiO_2 aerogel and xerogel composites *via* a one-pot sol–gel process at room temperature

Al-Zahraa Fatima El-Cheikh,[a] Witold Kwapinski,[a] Mohammad N. Ahmad,[b] James J. Leahy[a] and Houssam El-Rassy *[c]

A series of nanoporous ZnO/SiO_2 aerogels and xerogels were synthesized *via* an epoxide-assisted sol–gel route, aimed at producing zinc-rich composite materials with tunable properties. By systematically varying the zinc precursor, incorporating lithium chloride, and modifying the drying process, the resulting materials exhibited significant differences in crystallinity, morphology, and porosity. X-ray diffraction and FTIR analyses revealed primarily amorphous Zn–Si networks, with dispersed nanoscale crystalline phases, including zinc hydroxide nitrate, smithsonite, and simonkolleite. The incorporation of zinc into the silica matrix was achieved with stoichiometric control. Upon heat treatment, hydroxide phases were converted into mesoporous ZnO clusters, while preserving high surface areas and thermal stability. The aerogels showed low bulk density and open mesoporosity, whereas the xerogels exhibited enhanced structural robustness with similar surface areas. Optimized heat-treated aerogels reached surface areas up to 260 $m^2\ g^{-1}$, particle sizes down to 23 nm, and thermal stability beyond 800 °C. These findings confirm the successful design of hybrid Zn/SiO_2 nanomaterials with tunable architectures, positioning them as promising candidates for use in catalysis, adsorption, and thermal processing.

Received 24th July 2025
Accepted 10th October 2025

DOI: 10.1039/d5ra05345e

rsc.li/rsc-advances

Introduction

Zinc layered hydroxides (ZLHs) are a class of anionic clay-like materials, consisting of positively charged zinc hydroxide layers that are intercalated with various anions, including chloride, nitrate, or sulphate. Among these, simonkolleite ($Zn_5(OH)_8Cl_2 \cdot H_2O$) and zinc hydroxide nitrate ($Zn_5(OH)_8(NO_3)_2 \cdot 2H_2O$) have attracted considerable interest because of their distinctive physicochemical properties and their broad range of applications in both scientific and industrial fields.[1–3] Simultaneously, zinc oxide (ZnO) has gained interest as an exceptionally versatile material, known for its combination of piezoelectric and semiconducting properties. With a direct bandgap of 3.37 eV and a large exciton binding energy of 60 meV, ZnO demonstrates high efficiency in optoelectronic applications.[4–8] When combined, ZLHs and ZnO-based materials are extensively utilized in various applications, such as dye adsorption,[9,10] antibacterial coatings,[10,11] gas sensors,[12,13] UV-LEDs,[14] photocatalysis,[15] and more.[16] Their multifunctional properties and outstanding performance highlight their significance in advancing modern technologies and addressing critical challenges in materials science.

The development of customized ZLHs and ZnO-based nanocomposites is an emerging area of research focused on designing 3D structures with multifunctional properties, such as improved porosity and catalytic activity. Recent studies have highlighted the potential of nanocomposites like zinc layered hydroxide–salicylate,[17] and zinc oxide/silica,[18] particularly due to their mesoporous structures and enhanced functionalities. In this regard, sol–gel chemistry, using epoxide as a gelation agent, has become a valuable method for synthesizing mixed oxides nanocomposites. This approach enables precise control over the combination of multiple metal oxide phases at both the molecular and nanoscale levels, facilitating the development of advanced materials with specifically engineered properties.[19]

Zinc/silica composite aerogels and xerogels are distinctive three-dimensional network materials featuring interconnected nanoscale pores, extremely low density, large specific surface area, and high porosity.[20,21] These properties make them valuable for applications in fuel cells, photocatalysis, gas sensing, and as dielectrics.[21] The inclusion of silica improves mechanical stability and porosity, which makes these composites more desirable than pure zinc-based aerogels.[22] Typically, Zn–Si mixed oxides consist of zinc oxide encapsulated within a silicon oxide matrix, with silicon oxide being the major component in the composite. Zinc oxide content in Zn–Si composites is generally less than 20 wt%.[23] For instance, Chakrabarti *et al.*[24]

[a]*Department of Chemical and Environmental Science, University of Limerick, Limerick, Ireland*

[b]*Baha and Walid Bassatne Department of Chemical Engineering and Advanced Energy, American University of Beirut, Beirut, Lebanon*

[c]*Department of Chemistry, American University of Beirut, Beirut, Lebanon. E-mail: Houssam.Rassy@aub.edu.lb*

and Mocioiu *et al.*[25] prepared ZnO/SiO_2 composite films with silicon to zinc molar ratio of 20 : 80, while Bouguerra *et al.* used the sol–gel method to embed a small amount of ZnO nanocrystals in an amorphous SiO_2 matrix.[26] Despite previous studies on zinc-based aerogels, limited research exists on monolithic zinc-based aerogel materials where zinc is the primary component, and the influence of chloride ions on morphology remains poorly understood. Our goal is to synthesize a range of novel aerogels, air-dried xerogels, and heat-treated variants, where zinc is the major component and to investigate the effects of synthesis parameters and heat treatment on the final material structures.

In this study, we utilized a sol–gel approach to synthesize zinc/silica-based porous materials, combining zinc, a transition metal, with silica, a main-group metal, to create mixed metal oxide porous materials. Zinc/silica aerogels and xerogels were produced *via* an epoxide-driven sol–gel process, where tetramethyl-orthosilicate and zinc salts acted as the precursors.

One of the key benefits of this method is the use of zinc salts rather than zinc alkoxide, with epoxides initiating the co-polymerization of both zinc and silica species simultaneously. In parallel, conventional approaches often involve multiple distinct synthesis steps and require strong acids, strong bases, or elevated temperatures.[18,27–31] Our work introduces a novel one-pot, room-temperature sol–gel process that enables simultaneous co-gelation of zinc and silica, yielding a highly porous framework in which zinc is the dominant constituent. Epoxide facilitates the reaction by deprotonating the hydrated metal species, leading to the formation of oligomers from cationic metal species (both M–OH and Si–OH sites). These oligomers then link together through olation and oxolation to form metal–oxygen–metal bridges. As the sol undergoes further cross-linking, a monolithic gel is formed. The acidic metal salt solution catalyses condensation, enabling simultaneous gelation of both species.[32,33] We believe that this interaction plays a crucial role in the structural differences observed in the final materials. Specifically, the hydrolysis and condensation rates of each cationic metal species determine whether the structure is homogeneous or heterogeneous. These rates are influenced by the electrophilic nature of the metal salts (Cl^- or NO_3^-) and the presence of lithium chloride in the reaction medium, which alters the gelation dynamics.[34] When the hydrolysis and condensation rates of the zinc and silica precursors are well-matched, a homogeneous nanoscale structure (Zn–O–Si) is formed. However, when the rates are mismatched, phase separation occurs, resulting in heterogeneous structures where the condensed phase consists of interpenetrating networks of the two metal oxides, Zn–O–Zn and Si–O–Si. Alternatively, zinc oxides can exist as discrete nanoparticles.[22] Moreover, partial hydrolysis of zinc precursors leads to the formation of zinc nitrate hydroxide or zinc chloride hydroxide species, depending on the precursor used.[35] Zinc/silica composites could be divided into two categories based on the type of interaction between the zinc and silica phases, inspired by organic/inorganic hybrid aerogels.[36] As such, Category (a) composites will be those consisting of a heterogeneous structure where two phases of different nature are co-existing and held together by weak electrostatic forces, such as van der Waals forces or hydrogen bonding. On the other hand, Category (b) composites are homogeneous structures featuring strong chemical bonds (*e.g.*, Si–O–Zn bridging). Depending on intended applications, the use of porous amorphous materials could be beneficial. These materials may offer distinct advantages either in the presence or absence of crystalline zinc components.[37–41]

Zinc nitrate hexahydrate and zinc chloride were explored as zinc precursors in this study. We also investigated how the concentration of chloride ions in the sol affected the structure and morphology of the resulting material. Under certain conditions, the condensation reactions led to the formation of a homogeneous gel, enabling the successful preparation of a range of novel aerogels, air-dried xerogels, and heat-treated variants.

Materials and methods

Materials

All chemicals used in this study were used as received, without any further modification. Zinc(II) nitrate hexahydrate was obtained from Sigma-Aldrich. Zinc(II) chloride and zinc(II) acetate, purum, were supplied by Fluka Chemika. Tetramethyl orthosilicate (noted TMOS) and lithium chloride (purum) were from Fluka analytical, methanol (HPLC grade) from Honeywell International Inc., acetone (extra pure) from Scharlau, and propylene oxide (noted PO) from Acros Organics.

Synthesis materials

Metal stock solutions with a concentration of 0.64 M were prepared using methanol as the solvent. Both zinc(II) chloride and zinc(II) nitrate hexahydrate resulted in 0.64 M clear transparent solutions. In a typical synthesis, 2.5 mL of one of these metal stock solutions was mixed with 0.2 mL of tetramethyl orthosilicate (TMOS) in a propylene vial under magnetic stirring. To investigate the effect of lithium chloride, 0.2 mL of a 12 M LiCl aqueous solution was optionally added. Subsequently, 0.8 mL of propylene oxide (PO) was introduced, and stirring continued for 25 seconds, after which the gelation occurred. As gelation progressed, the initially colorless solution gradually turned cloudy and ultimately became white. The color transition is likely a result of structural changes during gel formation rather than any change in the oxidation state of zinc. Afterwards, the vials were then sealed and left for three days at room temperature for aging. No noticeable gel shrinkage was observed during this aging period.

Following the aging period, the gels were soaked in a bath of extra pure acetone to exchange residual solvents and pore-entrapped chemicals – including methanol, unreacted propylene oxide, and water – with acetone. It is important to note that the water present generated from the hydrated precursors. The acetone exchange step was carried out once daily over a period of three days.

To produce aerogels labelled as 'A', supercritical drying was performed using a critical point dryer from Quorum Technologies (Model E3100). The process began with exchanging the

Table 1 Sol–gel parameters for prepared aerogel and xerogel cases and their respective names

	Zinc precursor		12 M LiCl aq. solution		Drying process	
	Zinc nitrate	Zinc chloride	(0 mL)	(0.2 mL)	S.C.	Ambient
A/Si-Zn_{Nit}	*		*		*	
X/Si-Zn_{Nit}	*		*			*
A/Si-Zn_{Nit}(LiCl)	*			*	*	
X/Si-Zn_{Nit}(LiCl)	*			*		*
A/Si-Zn_{Chl}		*	*		*	
X/Si-Zn_{Chl}		*	*			*
A/Si-Zn_{Chl}(LiCl)		*		*	*	
X/Si-Zn_{Chl}(LiCl)		*		*		*

acetone in the gel pores with liquid CO_2 over five hours, during which the solvent was vented hourly. Afterwards, the temperature was gradually increased to 40 °C, surpassing the critical point of CO_2 ($T_c = 31$ °C; $P_c = 7.38$ MPa). The pressure was then slowly released over one hour until reaching back the atmospheric pressure, followed by cooling to room temperature. The resulting monolithic aerogels were then carefully retrieved. For xerogel production (labelled as 'X'), the acetone was simply decanted, and the gels were left to dry under ambient conditions for seven days.

The as-synthesized aerogels and xerogels were subjected to heat treatment in a muffle furnace at 400 °C. The heating ramp was set at 1 °C min^{-1} with a dwell time of 4 hours. No color changes were observed after the heat treatment.

The use of different sol–gel parameters yielded eight distinct aerogels and xerogels, identified as A or X/Si-$Zn_{Nit\ or\ Chl}$ (LiCl) depending on the synthesis parameters. 'Chl' refers to zinc chloride, 'Nit' to zinc nitrate hexahydrate, 'LiCl' indicates the use of LiCl in the synthesis, 'A' for aerogels, and 'X' for xerogels. A full list of these formulations is provided in Table 1, which summarizes the various synthetic conditions used. All aerogel powders maintained a fluffy appearance even after heat treatment. In contrast, the xerogels displayed a ceramic-like texture both before and after calcination.

Characterization materials

The bulk densities of as-synthesized monolithic aerogels and xerogels were calculated based on the measured mass-to-volume ratios of the individual monoliths.

The structural analysis was carried out using powder X-ray diffraction (XRD) on a BRUKER AXS diffractometer, the D8 Advance, fitted with Cu-Kα radiation (λ = 1.5406 Å). The measurements were performed across a 2θ range of 5° to 80°, with an increment of 0.02°, a voltage of 40 kV, a current of 40 mA, a power of 1.6 kW, and a counting time of 0.7 s per step. The diffraction data were visualized and analyzed using Power BI software. Phase identification was achieved by referencing digitized patterns from the International Center for Diffraction Data (ICDD) powder diffraction file (PDF) database. The degree of crystallinity was calculated by comparing the integrated area of the diffraction peaks to the total area in the diffractograms.

Scanning electron microscopy (SEM) was performed on a TESCAN MIRA3 LMU electron microscope at 25 kV equipped with an Oxford instruments energy dispersive X-ray spectroscopy (EDX) detector. Samples were first degassed at 50 °C for a minimum of 24 hours, then sputter-coated with a 12 nm layer of gold. Imaging was performed using backscattered electrons (BSE) detection which enhances contrast based on atomic number where heavier atoms like zinc appear brighter. This enables the differentiation between amorphous areas and crystalline zinc-rich phases.

Thermogravimetric analysis (TGA) was conducted using a NETZSCH TG 209 F1 Iris. The mass losses were tracked under nitrogen gas within a temperature range of 30 to 800 °C, with a heating rate of 5 °C min^{-1}. The slow scan rate was chosen to provide enhanced resolution of the transition allure. Approximately 3 mg of the aerogels samples were used, while 40 mg of the xerogels were analyzed.

Fourier-transform infrared (FTIR) spectroscopy was performed on a Bruker tensor 27 FT-IR spectrometer. Powdered aerogel and xerogel samples were analyzed using the diamond lens attenuated total reflectance (ATR) module (platinum ATR diamond F. vacuum, type: A225/Q). Spectral data were recorded in the 4000–400 cm^{-1} range.

Textural properties, including porosity and surface area, were evaluated through nitrogen adsorption–desorption isotherms at 77 K using a 3Flex Surface characterization analyzer (model ASAP 2015 from Micromeritics). The Brunauer–Emmett–Teller (BET) model was used to determine specific surface areas, while average pore diameter and pore volume were calculated using the desorption branch of the isotherm using the Barrett–Joyner–Halenda (BJH) and Dollimore–Heal models. Prior to analysis, powder samples were degassed at 120 °C for 24 hours to eliminate adsorbed gases and vapors. Each measurement required 24 hours, with an equilibrium interval of 30 seconds, extended to 55 seconds for samples expected to exhibit microporosity to guarantee slower gas adsorption dynamics in tiny pores.

Results and discussion

The nature of the metal to ligand bond plays a significant role in stabilizing both the reaction and the co-gelation process with silica, which ultimately affects the gel transition process.[42] Previous studies mostly reported gel formation when chloride salts were used in the reaction.[43,44] However, gel formation was successfully observed in all tested cases, except for the Si-Zn_{Chl}

Table 2 Monolith densities of as-synthesized aerogels and xerogels

	Density (g cm^{-3})
A/Si-Zn_{Chl}(LiCl)	0.20
X/Si-Zn_{Chl}(LiCl)	1.50
A/Si-Zn_{Nit}	0.16
X/Si-Zn_{Nit}	1.90
A/Si-Zn_{Nit}(LiCl)	0.15
X/Si-Zn_{Nit}(LiCl)	1.00

case, where zinc chloride was used as the zinc precursor. In this case, precipitation occurred instead of gelation. It is worth mentioning that using zinc acetate as a zinc precursor also works according to our procedure. Furthermore, our preliminary findings suggest that the choice of solvent is crucial for stabilizing gel transition. We found that stable gels formed in a range of protic solvents, such as ethanol, DMSO, and methanol.[45] Both TEOS and TMOS can serve as silicon precursors, and we also found that increasing the silicon precursor by a factor of 1.5 factor is possible. In addition to the chemical nature of the precursors and solvents, the concentration of zinc salts also plays a key role in gel formation. For instance, we observed that reducing the concentration of hydrated zinc precursors in methanol to below 0.15 M led to precipitation instead of gelation. When using deionized (DI) water instead of LiCl aqueous solution, a stable gel, along with its corresponding aerogel and xerogel, was formed whenever zinc nitrate and zinc acetate was used. However, zinc chloride resulted in precipitation, and no gel was formed. Aerogels made with water instead of LiCl exhibited lower-quality characteristics, such as higher density and lower surface area. As for why adding LiCl enhanced the gelation process, one possibility is that the amount of counter-anion accelerates the epoxide ring opening reaction, as suggested by Gash *et al.*[19] Another potential explanation is that the presence of LiCl aqueous solution may have promoted the hydrolysis reaction due to its water content and helped regulate the pH increase during gelation by acting as a buffer.

Density measurements of the as-synthesized monolithic aerogels showed values ranging from 0.15 to 0.20 g cm^{-3}, while their xerogel analogs had densities exceeding 1.00 g cm^{-3} (Table 2). The xerogels were noticeably more robust monolithic materials, experiencing nearly 50% volume shrinkage during the drying process.

The low density of aerogels is strongly linked to their high porosity.[46,47] Achieving a low-density monolith in aerogels means that the gelation occurred uniformly, allowing the porous structure to form properly without collapsing during drying. This suggests a successful gelation process and the creation of a stable 3D network structure.[48] Low-density materials offer numerous advantages in various applications. For instance, in fluidized bed reactors, they are easier to fluidize, which promotes better mixing and interaction with gaseous or liquid reactants, ultimately enhancing reaction kinetics.[49] In batch processes, low-density catalysts contribute to improved suspension stability and reduced sedimentation, helping maintain consistent catalytic activity.[50]

Powder X-ray diffraction (XRD)

X-ray diffractograms for the aerogels and xerogels, both before and after heat treatment, are shown in Fig. 1: (a) A/Si-Zn_{Nit} and X/Si-Zn_{Nit}, and (b) A/Si-Zn_{Chl}(LiCl), X/Si-Zn_{Chl}(LiCl), A/Si-Zn_{Nit}(LiCl); and X/Si-Zn_{Nit}(LiCl). All samples show broad diffraction peaks at $2\theta = 6°$ and 13.5°, which correspond to the amorphous zinc–silica matrix. Additionally, a broad peak typically associated with pure silica matrix appears at $2\theta = 23°$.[23,51] However, the absence of this peak in the samples indicates that the structure is not just a simple sol–gel SiO_2 matrix. Instead, the broad peaks observed at lower angles suggest the formation of an amorphous network that combines both silica and zinc, implying that zinc has integrated into the silica structure, disrupting its regular matrix. The relatively low crystallinity (2–11%) of the as-prepared samples can likely be attributed to the low-temperature synthesis process.

Powder X-ray diffraction (XRD) patterns of the as-synthesized A/Si-Zn_{Nit}, X/Si-Zn_{Nit}, and X/Si-Zn_{Nit}(LiCl) samples exhibit a series of sharp peaks, which match the pattern for zinc hydroxide nitrate hydrate ($Zn_5(OH)_8(NO_3)_2 \cdot 2H_2O$).[52] This suggests that a layered zinc hydroxide nitrate-silica composite material was formed. After heat treatment in static air at 400 °C, this composite transforms into a zinc oxide–silica material, indicating the thermal decomposition of the hydroxide nitrate phase.

In contrast, the major phase in sample A/Si-Zn_{Nit}(LiCl) and A/Si-Zn_{Chl}(LiCl) was identified as smithsonite $ZnCO_3$ (PDF File # 010831765), with diffraction peaks at 25.0°, 32.5°, 38.7°, 42.8°, 51.4°, 53.7°, 62.1°, 66.1°, and 70.0°. This suggests that carbonization occurred during the supercritical (SC) drying process of the Si-Zn_{Nit}(LiCl) and A/Si-Zn_{Chl}(LiCl) gel, a phenomenon previously reported by Kemal.[53] The broad diffraction peaks in the XRD patterns suggest small crystalline particle sizes, as inferred from the Debye–Scherrer equation, indicating that the crystallites are in the nanoscale range.

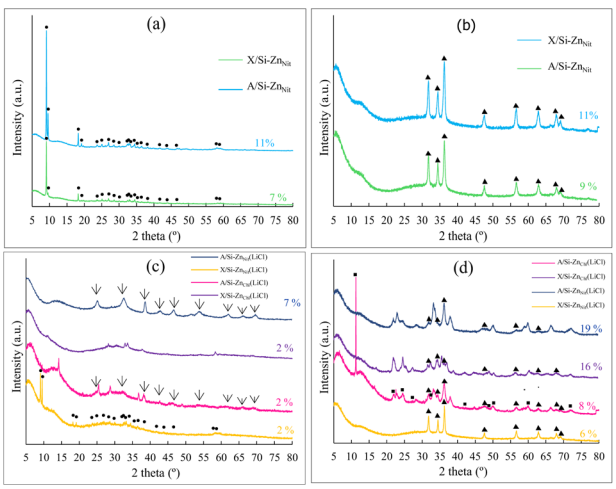

Fig. 1 X-ray diffraction patterns and the degree of crystallinity of A/Si-Zn_{Nit}, X/Si-Zn_{Nit} and X/Si-Zn_{Nit}(LiCl) and A/Si-Zn_{Chl}(LiCl), X/Si-Zn_{Chl}(LiCl), and A/Si-Zn_{Nit}(LiCl), before (a and c) and after heat treatment (b and d), respectively. The marked peaks correspond to $Zn_5(OH)_8(NO_3)_2 \cdot 2H_2O$ (●), ZnO (▲), $ZnCO_3$(↓) and $Zn_5(OH)_8Cl_2 \cdot H_2O$ (●).

Weak diffraction peaks were observed in the A/Si-Zn_{Chl}(LiCl) and X/Si-Zn_{Chl}(LiCl) samples, primarily indicating small amounts of crystalline zinc species, such as zinc hydrogen chloride hydrate ($ZnCl_2 \cdot HCl \cdot H_2O$, $2\theta = 14.1°$), zinc chloride ($ZnCl_2$, $2\theta = 25.2°$), and zinc peroxide (ZnO_2, $2\theta = 36.8°$). However, it was challenging to fully identify all the phases present. Despite this, the as-synthesized samples contain a significant amount of amorphous material, with other peaks representing minor products present in the samples.

After heat treatment, all samples exhibited diffraction peaks associated with zinc oxide at 31.8°, 34.4°, and 36.3°, corresponding to the lattice planes (100), (002), and (101), respectively. Additional peaks appeared at 17.5°, 56.6°, 62.8°, 66.4°, 67.9°, and 69.1°, which matched the lattice planes (102), (110), (103), (200), (112), and (201) (JCPDS: 36-1451), confirming the presence of ZnO clusters with a hexagonal wurtzite structure.

In addition to the ZnO formation, the X-ray diffraction pattern for A/Si-Zn_{Chl}(LiCl) showed the development of a simonkolleite crystalline phase during heat treatment.[3,54] Simonkolleite ($Zn_5(OH)_8Cl_2 \cdot H_2O$) diffraction peaks were observed at 11.2°, 16.6°, 22.2°, 22.5°, 24.5°, 28.7°, 30.4°, 31.0°, 32.8°, 33.2°, and 37.9°, while similar peaks in the X/Si-Zn_{Chl}(-LiCl) and A/Si-Zn_{Nit}(LiCl) patterns likely indicated other zinc chloride hydroxide species.

The formation of simonkolleite and other zinc chloride hydroxide species after heat treatment suggests that the samples initially contained an amorphous zinc-layered hydroxide phase, which crystallized upon heating. Zinc-based compounds can exist in either crystalline or amorphous forms, depending on the synthesis method.[55]

Heat treatment enhanced the crystallinity in all samples. However, for A/Si-Zn_{Nit} and X/Si-Zn_{Nit}, the formation of ZnO nanoparticles resulted in smaller particle sizes compared to the relatively larger zinc hydroxide nitrate clusters.

The presence of amorphous peaks at $2\theta = 6°$ and 13.5° in all samples, along with the low crystallinity observed both before and after heat treatment, indicates the formation of an amorphous silica–zinc 3D structure. This structure demonstrates high thermal stability, as it does not undergo crystallization during the heat treatment. This stability can likely be attributed to the formation of Zn–O–Si bridges, with SiO_2 preventing zinc from sintering and crystallizing.[56]

The amorphous fraction (ranging from 98% to 81%) is classified as a Category (b) nanocomposite where zinc remains well-dispersed within the amorphous silica matrix. In general, the material fits into Category (a) nanocomposites, where crystalline domains such as ZLHs and ZnO are physically embedded within an amorphous matrix.

Linking all synthesis parameters together to the obtained final phases, we found out that nitrate is the dominant counteranion in the sol when zinc nitrate is used without LiCl. Under limited hydrolysis, nitrate remains available to balance Zn^{2+}, thus promoting the formation of zinc layered hydroxide nitrate (ZLHN) within the structure.

When LiCl is added, chloride competes with nitrate for Zn^{2+} coordination, reducing the ZLHN fraction in the xerogel from ~7% to ~2%. In the aerogel, the ZLHN phase disappears, and carbonation is observed during supercritical CO_2 drying, suggesting that ZLHN is not stable under $scCO_2$ conditions.

For Si-Zn_{Chl}-LiCl, the aerogel shows a similar carbonation behavior whereas the corresponding xerogel (X/Si-Zn_{Chl}-LiCl) exhibits zinc chloride crystalline phases since chloride is the only strongly coordinating anion present. These phases appear to be unstable under $scCO_2$. An amorphous zinc–silica network forms in all cases.

Scanning electron microscopy (SEM)

SEM analysis of the samples A/Si-Zn_{Chl}(LiCl) and A/Si-Zn_{Nit}(-LiCl) reveals a similar morphology (Fig. 2a–c), with both samples consisting of homogeneously mixed thin flakes (petals) clusters and particle-like 3D structures. The petal-like clusters are similar to those observed in Zn(II) aerogels synthesized under similar conditions.[45,57] The as-synthesized xerogel X/Si-Zn_{Chl}(LiCl), shown in Fig. 2b, also features thin flakes, but they are clustered together to form spherical-like agglomerates, embedded within a heterogeneous particle-like 3D structure.

After heat treatment, the thin flakes develop cavities typical of mesoporous dimensions, while the overall particle-like morphology is maintained.

The heat-treated A/Si-Zn_{Chl}(LiCl) sample forms rod-shaped crystal clusters, identified as simonkolleite by X-ray diffraction (XRD) analysis. In contrast, its xerogel analogue, X/Si-Zn_{Chl}(-LiCl), exhibits smaller rod-shaped crystals. No distinct crystalline structures are observed in the heat-treated A/Si-Zn_{Nit}(LiCl) sample. Fig. 2d shows that the as-synthesized X/Si-Zn_{Nit}(LiCl) xerogel has a uniform amorphous structure composed of nanoscale spherical particles. After heat treatment, zinc oxide crystals migrate to the surface, forming clustered nanorods with an average size of about 1.5 μm.

As shown in Fig. 3a, the as-synthesized A/Si-Zn_{Nit} aerogel consists of crystalline phases embedded in a particulate-like amorphous matrix. The amorphous phase is composed of aggregated spherical nanoparticles (10–20 nm), forming an open mesoporous network, while the crystalline phase is made-up of hexagonal zinc hydroxide nitrate hydrate crystals clustered into flower-like aggregates (>4 μm).

Upon heat treatment, the amorphous phase remains stable, with no noticeable contraction of pores or growth of particles. However, the crystalline phase undergoes a distinct progeny effect, transforming into a mesoporous structure characterized by interconnected voids. This structural evolution is a clear indication of the thermal decomposition of zinc hydroxide nitrate into zinc oxide, as confirmed by XRD analysis.

The morphology of the corresponding xerogel (X/Si-Zn_{Nit}, Fig. 3b) differs from that of the aerogel primarily in its denser amorphous phase, which exhibits a significantly reduced pore volume. Nevertheless, similar hexagonal clusters of zinc hydroxide nitrate hydrate crystal are still present. Under heat treatment, the xerogel behaves in the same way as its aerogel counterpart.

In all cases, the observed 3D particle-like structure corresponds to the amorphous phase identified by XRD, which contains both silica and zinc components. After heat treatment,

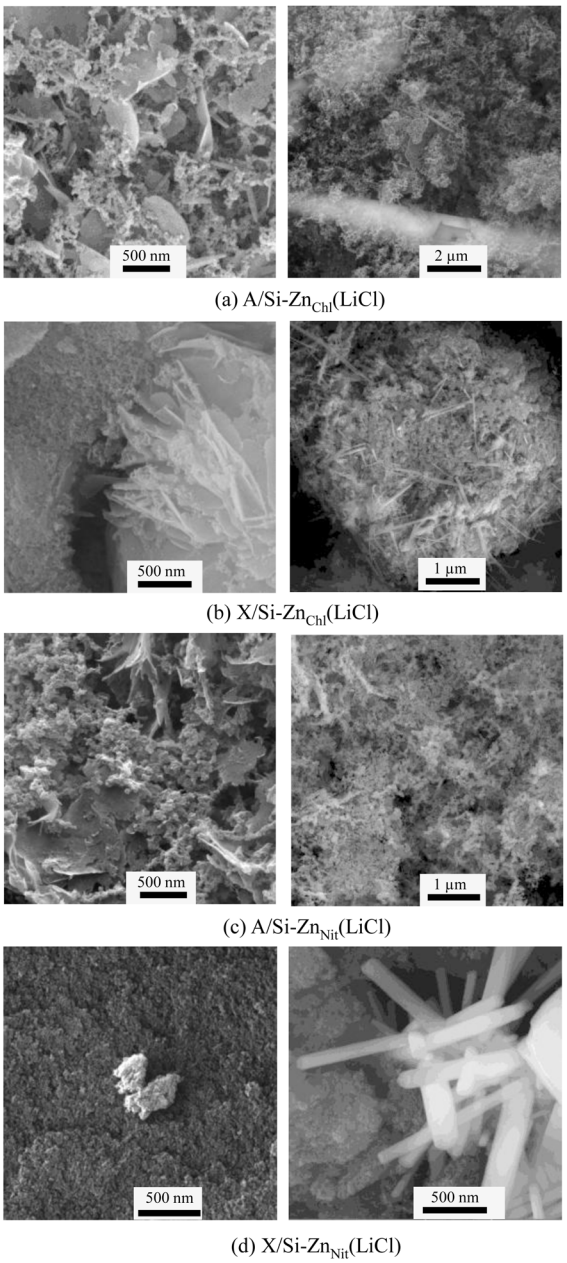

Fig. 2 SEM micrographs of as-synthesised (left) and 400 °C heat-treated (right). (a) A/Si-Zn$_{Chl}$(LiCl), (b) X/Si-Zn$_{Chl}$(LiCl), (c) A/Si-Zn$_{Nit}$(-LiCl) and (d) X/Si-Zn$_{Nit}$(LiCl) cases.

the samples exhibit zinc oxide in a variety of morphologies. This unique combination integrates the high selectivity and catalytic activity of crystalline ZnO along with the material's large surface area, thus enhancing its performance in applications such as photocatalysis and pollutant removal.[58,59]

Energy-dispersed X-ray (EDX) spectroscopy

EDX measurements performed on various random spots across the samples were used to determine the zinc-to-silica ratio, which was found to be nearly stoichiometric, ranging from 0.9 to 1.1 (Table 3). The Si/Zn ratios in both aerogels and xerogels

Table 3 Elemental composition analysis of as-synthesized and heat-treated aerogels and xerogels (atomic, %)

		Si	Zn	N	Cl
A/Si-Zn$_{Chl}$(LiCl)	As-synthesized	36	40	—	24
	Heat-treated	47	45	—	8
X/Si-Zn$_{Chl}$(LiCl)	As-synthesized	49	36	—	25
	Heat-treated	43	43	—	13
A/Si-Zn$_{Nit}$	As-synthesized	25	23	52	—
	Heat-treated	47	38	15	—
X/Si-Zn$_{Nit}$	As-synthesized	25	28	47	—
	Heat-treated	40	44	15	—
A/Si-Zn$_{Nit}$(LiCl)	As-synthesized	13	12	68	2
	Heat-treated	37	37	38	2
X/Si-Zn$_{Nit}$(LiCl)	As-synthesized	26	22	50	3
	Heat-treated	40	42	21	4

closely matched those of the starting solutions, indicating no significant zinc leaching occurred during synthesis.

Carbon, oxygen, nitrogen, and chlorine were also detected. Carbon and oxygen were removed due to interference from moisture and residual organic byproducts that were not fully eliminated during washing. The presence of nitrogen and chlorine in the heat-treated samples confirms that they are part of the thermally stable structure.

SEM-EDX elemental mapping (Fig. 4) confirmed the presence of Si and Zn in the A/Si-Zn$_{Nit}$ and A/Si-Zn$_{Chl}$(LiCl) composites. In the case of A/Si-Zn$_{Nit}$ (Fig. 4a), the EDX signals reveal a uniform distribution of zinc throughout the amorphous phase. The measured atomic ratio of zinc to silica (~3 : 7) further supports the successful incorporation of zinc into the

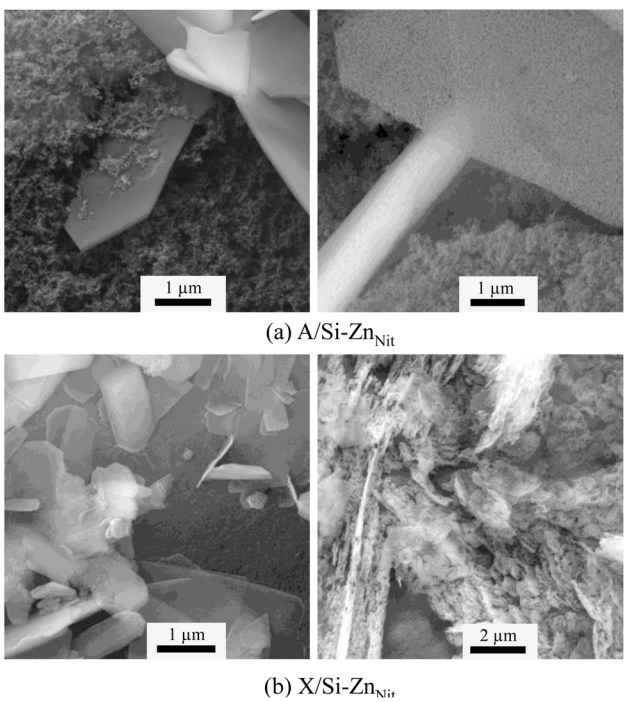

Fig. 3 SEM micrographs of as-synthesised (left) and 400 °C heat-treated (right). (a) A/Si-Zn$_{Nit}$ and (b) X/Si-Zn$_{Nit}$ cases.

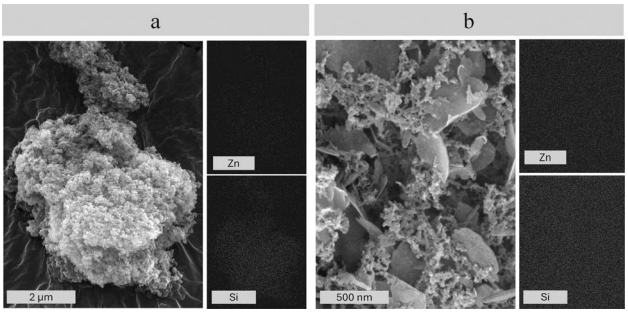

Fig. 4 Elemental mapping of zinc and silica in (a) A/Si-Zn_{Nit} (amorphous phase) and (b) A/Si-Zn_{Chl}(LiCl).

mesoporous matrix. Similarly, elemental mapping of A/Si-Zn_{Chl}(LiCl) shows a homogeneous distribution of both Si and Zn across the sample area.

Fourier-transform infrared (FTIR)

The four prominent peaks observed at 1060 cm^{-1}, 804 cm^{-1}, and 457 cm^{-1}, along with a shoulder peak at 975 cm^{-1}, are assigned to the asymmetric and symmetric stretching vibrations of Si–O–Si bridges, the Si–OH stretching vibration, and the bending vibration of Si–O–Si bonds, respectively.[20,60]

Fig. 5 shows the FTIR spectra of the aerogel samples. It should be noted that the FTIR spectra of the xerogels display similar spectral features to their corresponding aerogels in terms of peak positions. However, variations in peak intensities are observed, primarily for peaks associated with moisture, residual solvents, and ZnO highlighting differences in crystallinity between aerogels and their corresponding xerogels. These observations support theoretical expectations that the internal molecular-scale structure is primarily influenced by sol–gel synthesis conditions, with post-gelation drying methods exerting minimal influence.

The broad absorption band around 3450 cm^{-1} and the distinct peak around 1630 cm^{-1} are assigned to O–H stretching and H–O–H bending, respectively.[61] These peaks indicate the presence of moisture in both the as-synthesized and calcined samples, thus confirming the persistence of zinc-layered hydroxide structures.

As-synthesized A/Si-Zn_{Nit} exhibits the characteristic peaks of silica gel, each accompanied by a neighboring peak at slightly lower energies. These adjacent peaks suggest the incorporation of zinc into the silica matrix.[25,62,63] Additional peaks can be linked to zinc hydroxide nitrate and minor aerogel impurities.[64–66]

After heat treatment, the FTIR spectrum of A/Si-Zn_{Nit} shows the characteristic peaks of silica gel though broader and shifted toward lower energies. This behavior is indicative of a more pronounced incorporation of zinc into the silica network and increased structural defects within the silica matrix. No extra peaks appear in the spectrum, indicating the absence of zinc hydroxide nitrate and other impurities.

The presence of nitrogen detected by EDX, despite the absence of corresponding peaks in the FTIR spectrum, confirms its incorporation into the amorphous zinc–silica structure. This observation correlates with the thermal stability of the material, as no significant mass loss was observed beyond 400 °C (next section) indicating that the nitrogen species are structurally integrated and thermally stable within the zinc–silica network.

Both as-synthesized and heat-treated A/Si-Zn_{Nit}(LiCl) and A/Si-Zn_{Chl}(LiCl) exhibit similar behavior, although with more pronounced peak shifts indicating a higher degree of zinc incorporation into the silica matrix. A distinct ZnO-related peak is observed at 522 cm^{-1}.[67] The as-synthesized A/Si-Zn_{Nit}(LiCl) also displays peaks attributed to zinc carbonate species 'smithsonite',[68] while the heat-treated A/Si-Zn_{Chl}(LiCl) exhibits peaks corresponding to simonkolleite species. The persistence of O–H bands in these samples further supports the resilient zinc-layered hydroxide (simonkolleite) content retained within the structure.[68,69] In contrast, all other samples lack these features, indicating the absence of hydroxyl groups.

Thermogravimetric analysis (TGA)

The TGA profiles up to 800 °C and the corresponding derivative thermogravimetric (DTG) analysis under a dynamic nitrogen atmosphere are shown in Fig. 6a and b, respectively. The thermal decomposition behavior of both aerogel and xerogel

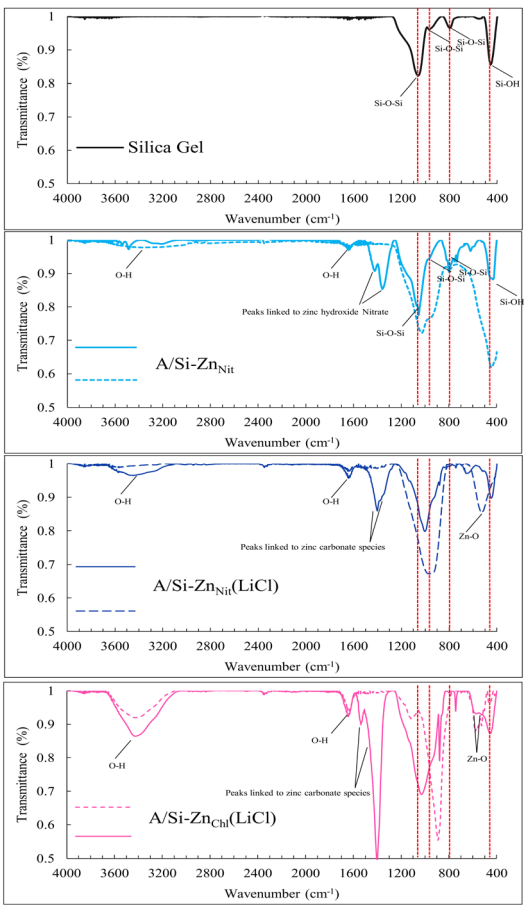

Fig. 5 FTIR spectra of the as-synthesized (solid lines) and heat-treated (dashed lines) aerogel samples, compared with the spectrum of pure commercial silica gel. Four vertical lines highlight the four characteristic silica gel peaks.

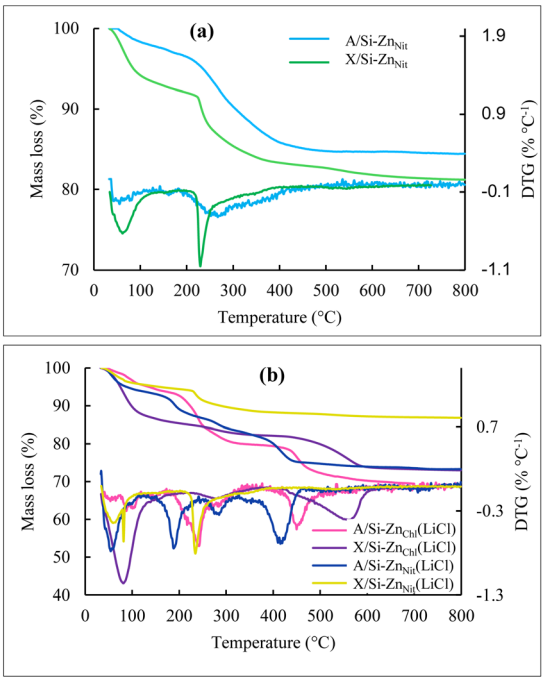

Fig. 6 TG and DTG analysis of (a) A/Si-Zn$_{Nit}$ and X/Si-Zn$_{Nit}$ and (b) A/Si-Zn$_{Chl}$(LiCl), X/Si-Zn$_{Chl}$(LiCl), A/Si-Zn$_{Nit}$(LiCl) and X/Si-Zn$_{Nit}$(LiCl) cases, under N_2 purge.

cases is highly influenced by the composite's internal structure, including the crystal phase and the nature of the interlayer anions, such as chloride or nitrate ions.

For all cases, an initial weight loss is observed below 100 °C, which is attributed to the evaporation of moisture and physically adsorbed residual solvents within the samples. Xerogels, in particular, are expected to retain a higher amount of residual solvents like methanol and acetone due to their microporous structure, which complicates solvent exchange and evaporation.

Samples such as X/Si-Zn$_{Nit}$(LiCl), A/Si-Zn$_{Nit}$ and X/Si-Zn$_{Nit}$, which contain a zinc hydroxide nitrate hydrate crystal phase embedded in an amorphous matrix, show a second mass loss between 200 °C and 400 °C. This loss is attributed to the oxidation of residual solvents, releasing CO, as well as the removal of interlayer water and hydroxyl groups. No further weight changes are observed up to the final measurement temperature. The total mass loss for these samples is 13%, 15%, and 20%, respectively.

The decomposition of zinc hydroxide nitrate hydrate into zinc oxide is believed to follow the reaction outlined in eqn (1), which accounts for the observed mass loss.[52,70] Energy-dispersive X-ray spectroscopy (EDX) confirms the presence of nitrate anions in the structure. However, the absence of hydroxide peaks in the ATR spectra of the heat-treated samples suggests that no zinc hydroxide nitrate species remain after treatment.

$$Zn_3(OH)_4(NO_3)_2\cdot 2H_2O \rightarrow 3ZnO + 2HNO_3 + 3H_2O \quad (1)$$

The samples A/Si-Zn$_{Nit}$(LiCl), A/Si-Zn$_{Chl}$(LiCl), and X/Si-Zn$_{Chl}$(LiCl) show similar second-stage mass losses between 200 °C and 400 °C, with minor variations in the onset temperatures. Notably, each sample exhibits a third distinct mass loss at progressively higher temperatures: 415 °C for A/Si-Zn$_{Nit}$(LiCl), 450 °C for A/Si-Zn$_{Chl}$(LiCl), and 550 °C for X/Si-Zn$_{Chl}$(LiCl). The total weight losses for these samples are 23%, 23%, and 30%, respectively. ATR spectra of the heat-treated samples at 400 °C show an O–H stretching band, indicating the presence of residual $Zn_5(OH)_8Cl_2\cdot H_2O$. Therefore, the third mass loss is attributed to the further thermal decomposition of both

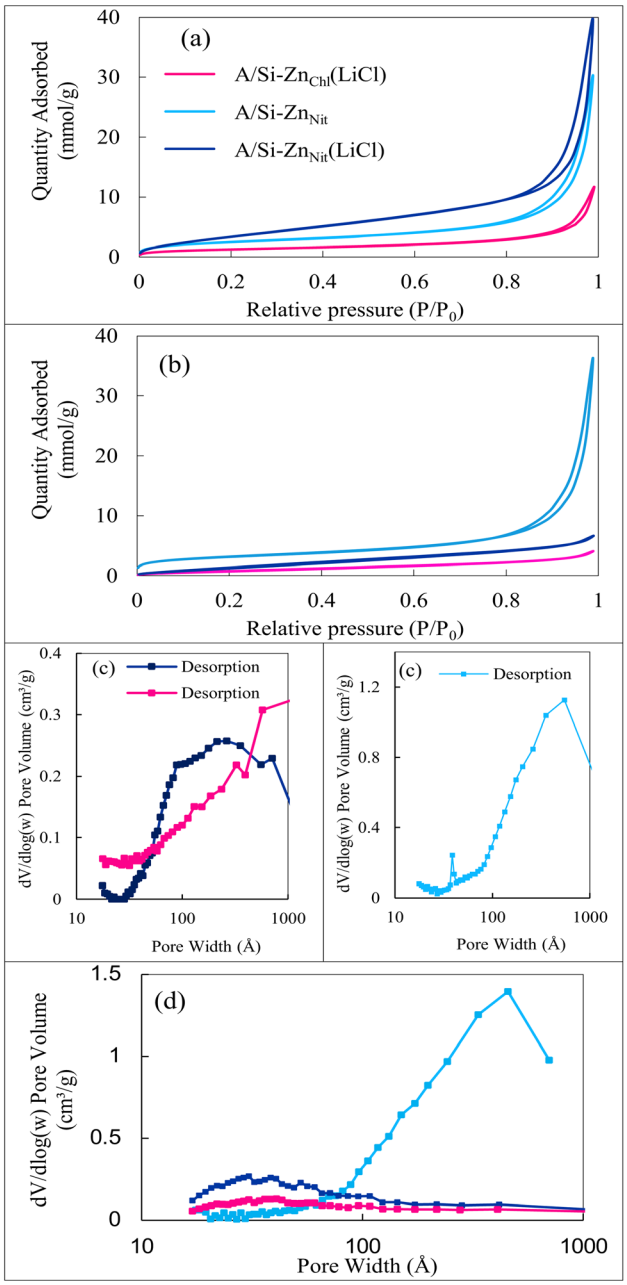

Fig. 7 Nitrogen physisorption isotherm and the pore size distribution of (a, c) the as-synthesized and (b, d) the heat-treated cases A/Si-Zn$_{Nit}$, A/Si-Zn$_{Chl}$(LiCl) and A/Si-Zn$_{Nit}$(LiCl) respectively.

crystalline and amorphous forms of $Zn_5(OH)_8Cl_2 \cdot H_2O$ into ZnO, as shown in eqn (2).[71]

$$Zn_5(OH)_8Cl_2 \cdot H_2O \rightarrow 5ZnO + 2HCl + 4H_2O \quad (2)$$

The pre- and post-heat treatment EDX analysis of nitrogen and chlorine can be correlated with the mass losses observed below 400 °C, where nitrogen and chlorine are oxidized, contributing significantly to the overall mass loss.

In addition to the solvent content within the pores, the decomposition behavior is influenced by the drying method—whether ambient drying or supercritical CO_2 extraction—especially when the network structure is not well developed. In such cases, the aerogel may exhibit lower thermal stability compared to its xerogel counterpart, as observed in the case of A/Si-Zn_{Nit}(LiCl). The more open and fragile structure of the aerogel is more susceptible to structural deformation upon heating than the denser, more compact xerogel structure.

Nitrogen adsorption–desorption

Nitrogen adsorption–desorption isotherms and pore size distributions of the aerogels before and after heat treatment are shown in Fig. 7, while Fig. 8 shows their corresponding data for the xerogels. Table 4 summarizes the BET surface area, pore volume, average pore size, and average particle size for each sample. The pore size distributions were derived using the Dollimore–Heal (DH) method.

All samples exhibit type IV isotherms indicative of the mesoporous nature of the materials, and display hysteresis loops associated with the capillary condensation within the mesopores. The steep increase in adsorption at relatively high pressures P/P_0 for the as-synthesized A/Si-Zn_{Nit}, A/Si-Zn_{Nit}(LiCl), A/Si-Zn_{Chl}(LiCl), and X/Si-Zn_{Chl}(LiCl) suggests the presence of larger mesopores and macropores.[72] In contrast, the isotherms of as-synthesized X/Si-Zn_{Nit} and X/Si-Zn_{Nit}(LiCl) show saturation at high pressure revealing a narrower pore structure. Additionally, the plateau at relatively low pressure (starting from $P/P_0 = 0.001$) indicates the filling of micropores. These findings highlight the featured porosity of these aerogels and xerogels where micropores, mesopores, and macropores are presented.[26,73]

The as-synthesized aerogels generally feature H3-type hysteresis loops, which are associated with the metastability of adsorbed multilayer, low degree of pore curvature (less tortuosity), and nonrigidity of the aggregate structure.[72] However, X/Si-Zn_{Nit}(LiCl), and X/Si-Zn_{Chl}(LiCl), show H1-type hysteresis loops, associated with porous materials consisting of agglomerates of compact uniform spheres. On the other hand, xerogel X/Si-Zn_{Nit} shows H2(b) hysteresis loop associated with percolation effects due to a network structure consisting of ink-bottle-shaped micropores. The significant difference between the adsorption and desorption traces in the pore size distribution supports this interpretation, with a desorption peak at 75 Å corresponding to the narrow pore necks. This structure is associated with the complex pore connectivity which can trap the adsorbate during desorption, particularly around $P/P_0 = 0.8$ (Fig. 8).

After heat treatment, the samples that retained Type IV isotherms (Fig. 7 and Fig. 8) indicate that their characteristic or multi-scale porosities remained largely unaffected, pointing to the microstructural stability of the materials. However, certain samples such as X/Si-Zn_{Chl}(LiCl) did not exhibit the same thermal stability, losing up to 80% of their specific surface area under particular synthesis conditions (Table 4).

Overall, the pore size distributions of all samples are within the mesoporous range of 20 to 100 Å.

Overall, the aerogels exhibit high surface areas and pore diameters predominantly within the mesopore region, with average particle sizes as small as 19 nm. The xerogels show comparable surface areas, though with a noticeable reduction in pore volume, likely reflecting a denser overall morphology.

Most of the heat-treated analogues maintain surface areas comparable to their original counterparts, indicating good thermal stability. Although, A/Si-Zn_{Nit} shows an increase in specific surface area from 208 $m^2\ g^{-1}$ to 260 $m^2\ g^{-1}$.

The pore width distribution shows minimal changes in both cases, while the pore volume experiences a slight decrease. The consistency in average pore diameters confirms that the structures are resistant against aggregation and sintering during

Table 4 Physical properties of prepared aerogels and xerogels before and after heat treatment

		BET surface area ($m^2\ g^{-1}$)	BJH pore volume ($cm^3\ g^{-1}$)	BJH average radius (Å)	Average particle size (Å)
A/Si-Zn_{Chl}(LiCl)	As-synthesized	105	0.4	89	57
	Heat-treated	82	0.1	70	77
X/Si-Zn_{Chl}(LiCl)	As-synthesized	125	0.7	87	47
	Heat-treated	24	0.1	175	252
A/Si-Zn_{Nit}	As-synthesized	208	1.0	113	28
	Heat-treated	260	1.2	125	23
X/Si-Zn_{Nit}	As-synthesized	266	0.5	31	22
	Heat-treated	220	0.4	31	27
A/Si-Zn_{Nit}(LiCl)	As-synthesized	335	1.3	153	19
	Heat-treated	163	0.2	59	36
X/Si-Zn_{Nit}(LiCl)	As-synthesized	217	0.8	61	27
	Heat-treated	146	0.5	61	41

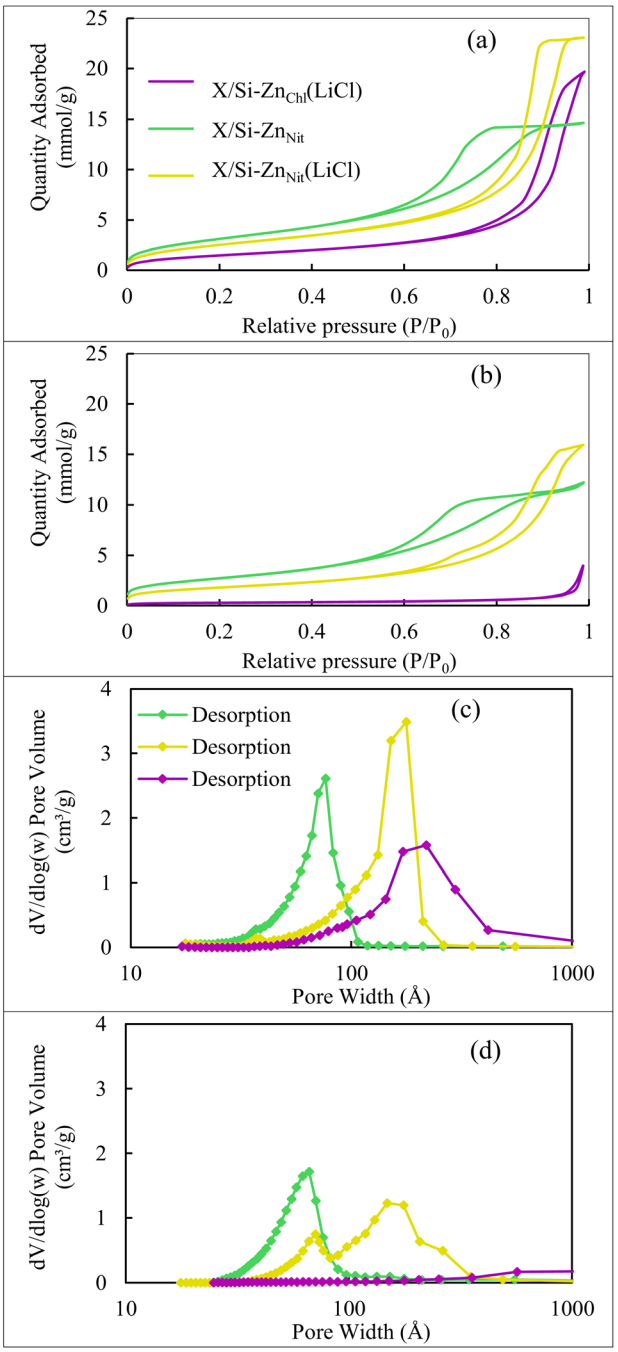

Fig. 8 Nitrogen physisorption isotherm and the pore size distribution of (a, c) the as-synthesized and (b, d) the heat-treated cases X/Si-Zn$_{Nit}$, X/Si-Zn$_{Chl}$(LiCl) and X/Si-Zn$_{Nit}$(LiCl) respectively.

heat treatment. The average pore diameter of samples A/Si-Zn$_{Chl}$(LiCl) and X/Si-Zn$_{Nit}$(LiCl) revealed some reduction (from 89 Å to 70 Å and from 153 Å to 59 Å, respectively), likely due to cavity formation within the pallets. While heat treatment tends to increase the average particle size, some samples remain in the nanoscale range, measuring around 23 nm. The surface areas measured before and after heat treatment are higher than previously reported values for ZnO nanoparticles synthesized by the sol–gel route.[45,74]

The high surface area observed for calcined A/Si-Zn$_{Nit}$ can be attributed to two factors. First is the thermal stability of its amorphous particle-like 3D structure, where zinc incorporated as Zn–O–Si bridges does not undergo sintering during heat treatment. Second is the formation of mesopores within the macro-sized zinc nitrate hydroxide crystals, resulting in a mesoporous zinc oxide structure (Fig. 7).

The structural stability of the aerogels and xerogels is indicated by the residual mass from thermal analysis and the surface area retained after heat treatment. Greater mass loss coupled with larger surface-area decreases correlates with a less stable framework. Across all samples, LiCl-free composites are the most robust, attributable to the network established during synthesis. Aerogels are generally more stable than xerogels, because ambient drying of xerogels induces structural collapse (rupture/shrinkage) and consequent loss of porosity.

Conclusion

A series of Zn/SiO$_2$ aerogel and xerogel composites were developed using a tailored sol–gel synthesis approach. Through a systematic investigation of parameters, such as zinc precursor type, the presence of aqueous lithium chloride, drying techniques, and heat treatment, it was found that these variables significantly impact the materials' structural, textural, and morphological characteristics.

Specifically, using zinc nitrate hexahydrate under controlled conditions led to the formation of well-crystallized zinc hydroxide nitrate hydrate (ZLHs) with distinctive flower-like morphology, embedded within a mesoporous, thermally stable amorphous zinc–silica matrix, classifying it as composite (a). Upon thermal treatment, the decomposition of ZLHs to zinc oxide created mesoporous cavities, enhancing specific surface area (SSA), pore volume, and thermal stability, as evidenced by minimal mass loss above 400 °C in TGA analyses.

The addition of aqueous lithium chloride facilitated gelation with zinc chloride precursors, yielding predominantly amorphous zinc–silica matrices with homogeneously dispersed smithsonite ($ZnCO_3$) crystals, observed only in aerogels, indicating carbonization during the supercritical drying. Upon calcination, an unexpected simonkolleite crystalline phase emerged in A/Si-Zn$_{Chl}$(LiCl), producing a unique dual-crystalline-phase material with intriguing morphology.

Ambient drying processes resulted in denser xerogels with comparable SSA to aerogels, despite higher bulk density. The slower drying conditions induced a lower crystallinity, which enhanced structural stability and thermal resilience. This more economical process presents xerogels as practical alternatives for aerogels in certain applications. However, the low-density aerogels, resulting from uniform gelation and supercritical drying, are particularly suited for applications requiring lightweight, highly porous materials such as fluidized systems, thermal insulation, or filtration.

Additionally, a notable zinc oxide surface migration phenomenon was observed in X/Si-Zn$_{Nit}$(LiCl) during heat treatment. Despite potential sintering effects and reduced porosity, the material still retained a high SSA of 146 m^2 g^{-1}.

Evidence from structural characterization indicates the formation of a 3D amorphous silica–zinc network, with Zn–O–Si bridging entities, categorizing these materials partially as Category (b) composites.

However, cases where zinc species observed as macroscale, the overall material is counted as Category (a). The tailored epoxide-assisted gelation method demonstrated clear advantages, enabling precise control over porosity types and structural properties at the nanoscale, thus offering materials with optimized multi-scale porosity suitable for various applications.

Data availability

The authors confirm that the data supporting the findings of this study are available within the article.

Conflicts of interest

There are no conflicts to declare.

Acknowledgements

This project is a collaborative effort between the American University of Beirut and the University of Limerick. The authors acknowledge the Kamal A. Shair Central Research Science Laboratory, Faculty of Arts and Sciences at the American University of Beirut, for the research facilities provided. Special thanks to Miss Rania Chatila for support with the experimental work.

References

1 Z. Gu, J. J. Atherton and Z. P. Xu, *Chem. Commun.*, 2015, **51**, 3024–3036.
2 N. Hahsim, Z. Muda, I. Md Isa, N. Abu Bakar, W. R. Wan Mahamod, N. Mohd Ali, S. N. Mohd Sharif, M. N. Jajuli, S. A. Mohd Zobir and S. Suyanta, *Indones. J. Chem.*, 2023, **23**, 881–898.
3 Y. Li, Y. Zou and Y. Hou, *Cryst. Res. Technol.*, 2011, **46**, 305–308.
4 M. Zhi, L. Zhu, Z. Ye, F. Wang and B. Zhao, *J. Phys. Chem. B*, 2005, **109**, 23930–23934.
5 P. Gao and Z. L. Wang, *J. Phys. Chem. B*, 2002, **106**, 12653–12658.
6 M. H. Koch, A. J. Hartmann, R. N. Lamb, M. Neuber and M. Grunze, *J. Phys. Chem. B*, 1997, **101**, 8231–8236.
7 X. Wang, C. J. Summers and Z. L. Wang, *Nano Lett.*, 2004, **4**, 423–426.
8 T. Gao, Q. Li and T. Wang, *Chem. Mater.*, 2005, **17**, 887–892.
9 K. Keis, J. Lindgren, S.-E. Lindquist and A. Hagfeldt, *Langmuir*, 2000, **16**, 4688–4694.
10 J. Cao, Y. Li, X. Chen, D. Cai, S.-F. Zhou and G. Zhan, *Mater. Today Commun.*, 2022, **31**, 103650.
11 C. Velázquez-Carriles, M. E. Macías-Rodríguez, O. Ramírez-Alvarado, R. I. Corona-González, A. Macías-Lamas, I. García-Vera, A. Cavazos-Garduño, Z. Villagrán and J. M. Silva-Jara, *Molecules*, 2022, **27**, 6161.
12 H.-M. Lin, S.-J. Tzeng, P.-J. Hsiau and W.-L. Tsai, *Nanostruct. Mater.*, 1998, **10**, 465–477.
13 S. Polarz, A. Roy, M. Lehmann, M. Driess, F. E. Kruis, A. Hoffmann and P. Zimmer, *Adv. Funct. Mater.*, 2007, **17**, 1385–1391.
14 D. C. Look and B. Claflin, *Phys. Status Solidi B*, 2004, **241**, 624–630.
15 A. Umar, V. Sabrina and Y. Yulizar, *Inorg. Chem. Commun.*, 2022, **141**, 109593.
16 D. R. Clarke, *J. Am. Ceram. Soc.*, 1999, **82**, 485–502.
17 M. Ramli, M. Z. Hussein and K. Yusoff, *Int. J. Nanomed.*, 2013, **8**, 297–306.
18 W. Widiyastuti, I. Maula, T. Nurtono, F. Taufany, S. Machmudah, S. Winardi and C. Panatarani, *Chem. Eng. J.*, 2014, **254**, 252–258.
19 A. E. Gash, T. M. Tillotson, J. H. Satcher Jr, L. W. Hrubesh and R. L. Simpson, *J. Non-Cryst. Solids*, 2001, **285**, 22–28.
20 A. C. Pierre and G. M. Pajonk, *Chem. Rev.*, 2002, **102**, 4243–4266.
21 D. R. Rolison and B. Dunn, *J. Mater. Chem.*, 2001, **11**, 963–980.
22 A. C. Pierre and A. Rigacci, *Aerogels Handbook*, Springer, New York, NY, 1 edn, 2011.
23 H. Haiping, W. Yuxia and Z. Youming, *J. Phys. D: Appl. Phys.*, 2003, **36**, 2972–2975.
24 S. Chakrabarti, D. Ganguli and S. Chaudhuri, *J. Phys. D: Appl. Phys.*, 2003, **36**, 146–151.
25 O.-C. Mocioiu, C. M. Vlădu□, I. Atkinson, V. Brătan and A.-M. Mocioiu, *Gels*, 2022, **8**, 498.
26 M. Bouguerra, M. Samah, M. A. Belkhir, A. Chergui, L. Gerbous, G. Nouet, D. Chateigner and R. Madelon, *Chem. Phys. Lett.*, 2006, **425**, 77–81.
27 G. Liu, Z.-H. Huang and F. Kang, *J. Hazard. Mater.*, 2012, **215–216**, 166–172.
28 A. B. Abou Hammad, A. M. Mansour, A. M. Bakr and A. M. El Nahrawy, *Egypt. J. Chem.*, 2022, **65**, 163–171.
29 E. A. Straumal, I. O. Gozhikova, S. Y. Kottsov and S. A. Lermontov, *Russ. J. Inorg. Chem.*, 2022, **67**, 1646–1651.
30 D. P. Debecker and P. H. Mutin, *Chem. Soc. Rev.*, 2012, **41**, 3624–3650.
31 A. Feinle and N. Hüsing, *J. Supercrit. Fluids*, 2015, **106**, 2–8.
32 L. Bourget, D. Leclercq and A. Vioux, *J. Sol-Gel Sci. Technol.*, 1999, **14**, 137–147.
33 P. Arnal, R. J. P. Corriu, D. Leclercq, P. H. Mutin and A. Vioux, *MRS Proc.*, 1994, **346**, 339.
34 G. Piccaluga, *Sol-gel Preparation and Characterization of Metal-Silica and Metal Oxide-Silica Nanocomposites*, Trans Tech Publications, 2000.
35 G. Guerrero, P. H. Mutin and A. Vioux, *Chem. Mater.*, 2000, **12**, 1268–1272.
36 P. Meti, D. B. Mahadik, K.-Y. Lee, Q. Wang, K. Kanamori, Y.-D. Gong and H.-H. Park, *Mater. Des.*, 2022, **222**, 111091.
37 K. Sinko, *Materials*, 2010, **3**, 704–740.
38 M. Gu, L. Hao, Y. Wang, X. Li, Y. Chen, W. Li and L. Jiang, *Chem. Phys.*, 2020, **534**, 110750.
39 J. Zhao, X. Yuan, X. Wu, L. Liu, H. Guo, K. Xu, L. Zhang and G. Du, *Molecules*, 2023, **28**, 3541.

40 M. Zaimee, M. Sarjadi and M. L. Rahman, *Water*, 2021, **13**(19), 2659.
41 F. Akhter, S. A. Soomro and V. J. Inglezakis, *J. Porous Mater.*, 2021, **28**, 1387–1400.
42 G. Picci, C. Caltagirone, A. Garau, V. Lippolis, J. Milia and J. W. Steed, *Coord. Chem. Rev.*, 2023, **492**, 215225.
43 *Chemistry of the Elements*, ed. N. N. Greenwood and A. Earnshaw, Butterworth-Heinemann, Oxford, 2nd edn, 1997, pp. 1201–1226.
44 C. N. Sisk and L. J. Hope-Weeks, *J. Mater. Chem.*, 2008, **18**, 2607–2610.
45 Y. P. Gao, C. N. Sisk and L. J. Hope-Weeks, *Chem. Mater.*, 2007, **19**, 6007–6011.
46 E. Barrios, D. Fox, Y. Y. Li Sip, R. Catarata, J. E. Calderon, N. Azim, S. Afrin, Z. Zhang and L. Zhai, *Polymers*, 2019, **11**, 726.
47 A.-G. Niculescu, D.-I. Tudorache, M. Bocioagă, D. E. Mihaiescu, T. Hadibarata and A. M. Grumezescu, *Nanomaterials*, 2024, **14**, 469.
48 S. Dervin and S. C. Pillai, in *Sol–Gel Materials for Energy, Environment and Electronic Applications*, ed. S. C. Pillai and S. Hehir, Springer International Publishing, 2017, pp. 1–22.
49 J. Balag, D. A. Franco, V. G. Miral, V. Reyes, L. J. Tongco and E. C. R. Lopez, *Eng. Proc.*, 2023, **56**, 62.
50 F. Akhter, M. Pinjaro, J. Ahmed, M. Ahmed, E. H. Arain, M. Ahsan and I. Sanjrani, *Biomass Convers. Biorefin.*, 2025, **15**, 6585–6614.
51 G. Li, T. Zhu, Z. Deng, Y. Zhang, F. Jiao and H. Zheng, *Chin. Sci. Bull.*, 2011, **56**, 685–690.
52 T. Ramesh and T. Madhu, *Int. J. Inorg. Chem.*, 2015, **2015**, 1–11.
53 I. Singh and K. Celik, *J. CO_2 Util.*, 2023, **79**, 102657.
54 S. Cousy, N. Reinders, L. Svoboda and J. Zelenka, *Chem. Pap.*, 2017, **71**, 1–10.
55 Y.-H. Gao, Z.-H. Liu and X.-L. Wang, *J. Chem. Thermodyn.*, 2009, **41**, 775–778.
56 J. B. Miller, S. E. Rankin and E. I. Ko, *J. Catal.*, 1994, **148**, 673–682.
57 R. M. Allaf and L. J. Hope-Weeks, *J. Nanomater.*, 2014, **2014**, 491817.
58 T. Y. Shvareva, S. V. Ushakov, A. Navrotsky, J. A. Libera and J. W. Elam, *J. Mater. Res.*, 2008, **23**, 1907–1915.
59 A. Herzog, M. Rüscher, H. S. Jeon, J. Timoshenko, C. Rettenmaier, U. Hejral, E. M. Davis, F. T. Haase, D. Kordus, S. Kühl, W. Frandsen, A. Bergmann and B. Roldan Cuenya, *Energy Environ. Sci.*, 2024, **17**, 7081–7096.
60 B. J. Clapsaddle, A. E. Gash, J. H. Satcher and R. L. Simpson, *J. Non-Cryst. Solids*, 2003, **331**, 190–201.
61 D. A. Long, *J. Raman Spectrosc.*, 2004, **35**, 905.
62 M. Cozzolino, M. Di Serio, R. Tesser and E. Santacesaria, *Appl. Catal., A*, 2007, **325**, 256–262.
63 A. Barhoum, G. Van Assche, H. Rahier, M. Fleisch, S. Bals, M.-P. Delplancked, F. Leroux and D. Bahnemann, *Mater. Des.*, 2017, **119**, 270–276.
64 D. A. Nogueira, T. M. Zanela, M. V. Machado, C. A. Almeida and R. Marangoni, *Colorants*, 2023, **2**, 565–577.
65 R. Bull, C. Markland, G. Williams and D. O'Hare, *J. Mater. Chem.*, 2011, **21**, 1822–1828.
66 N. Nityashree and M. Rajamathi, *J. Phys. Chem. Solids*, 2013, **74**, 1164–1168.
67 A. Kaningini, S. Azizi, N. Sintwa, K. Mokalane, K. Mohale, F. Mudau and M. Maaza, *ACS Omega*, 2022, **7**, 31658–31666.
68 J. Winiarski, W. Tylus, K. Winiarska, I. Szczygieł and B. Szczygieł, *J. Spectrosc.*, 2018, **2018**, 2079278.
69 F. Zhu, D. Persson, D. Thierry and C. Taxén, *Corrosion*, 2000, **56**, 1256–1265.
70 A. Moezzi, P.-S. Lee, A. M. McDonagh and M. B. Cortie, *J. Solid State Chem.*, 2020, **286**, 121311.
71 A. Moezzi, M. Cortie and A. McDonagh, *Dalton Trans.*, 2016, **45**, 7385–7390.
72 M. Thommes, K. Kaneko, A. V. Neimark, J. P. Olivier, F. Rodriguez-Reinoso, J. Rouquerol and K. S. W. Sing, *Pure Appl. Chem.*, 2015, **87**, 1051–1069.
73 B. Liu, M. Gao, X. Liu, X. Zhao, J. Zhang and X. Yi, *ACS Appl. Nano Mater.*, 2019, **2**, 7299–7310.
74 M. Krumm, C. L. Pueyo and S. Polarz, *Chem. Mater.*, 2010, **22**, 5129–5136.